Stability of Monodisperse Phospholipid-Coated Microbubbles Formed by Flow-Focusing at High Production Rates

Tim Segers,*,[†] Leonie de Rond,[†] Nico de Jong,[‡] Mark Borden,[§] and Michel Versluis[†]

[†]Physics of Fluids Group, MESA+ Institute for Nanotechnology, and MIRA Institute for Biomedical Technology and Technical Medicine, University of Twente, P. O. Box 217, 7500 AE Enschede, The Netherlands

[‡]Department of Biomedical Engineering, Thoraxcenter, Erasmus MC, Wyternaweg 80 EE 2302, 3015 CN Rotterdam, The Netherlands

[§]Department of Mechanical Engineering, University of Colorado, 1111 Engineering Drive, Boulder, Colorado 80309-0427, United States

ⓢ *Supporting Information*

ABSTRACT: Monodisperse microbubble ultrasound contrast agents may dramatically increase the sensitivity and efficiency in ultrasound imaging and therapy. They can be produced directly in a microfluidic flow-focusing device, but questions remain as to the interfacial chemistry, such as the formation and development of the phospholipid monolayer coating over time. Here, we demonstrate the synthesis of monodisperse bubbles with radii of 2−10 μm at production rates ranging from 10^4 to 10^6 bubbles/s. All bubbles were found to dissolve to a stable final radius 2.55 times smaller than their initial radius, independent of the nozzle size and shear rate, indicating that the monolayer self-assembles prior to leaving the nozzle. The corresponding decrease in surface area by a factor 6.6 reveals that lipid molecules are adsorbed to the gas−liquid interface in the disordered expanded state, and they become mechanically compressed by Laplace pressure-driven bubble dissolution to a more ordered condensed state with near zero surface tension. Acoustic characterization of the stabilized microbubbles revealed that their shell stiffness gradually increased from 0.8 to 2.5 N/m with increasing number of insonations through the selective loss of the more soluble lipopolymer molecules. This work therefore demonstrates high-throughput production of clinically relevant monodisperse contrast microbubbles with excellent control over phospholipid monolayer elasticity and microbubble resonance.
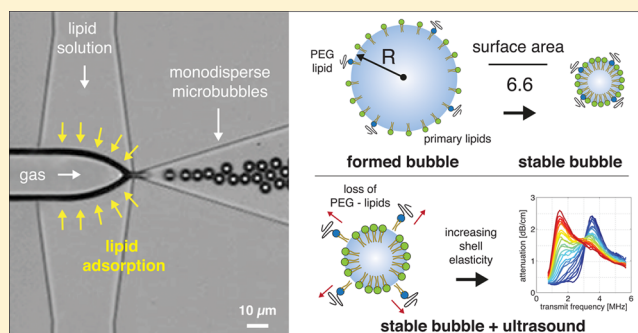
1. INTRODUCTION

An ultrasound contrast agent (UCA) typically consists of a suspension of phospholipid-coated microbubbles with radii ranging from 1 to 10 μm that scatter ultrasound more efficiently than red blood cells and tissues owing to the large compressibility of the microbubble gas core. The bubbles oscillate nonlinearly in response to a driving ultrasound field,[1] and the nonlinear echo allows for the visualization and quantification of organ perfusion.[2] The radial bubble response is governed by a strong coupling between the microbubble size and the driving frequency through the eigenfrequency of the bubble.[3] Clinical ultrasound systems, however, typically operate at a frequency bandwidth that is relatively narrow as compared to the bubble resonance frequencies in a typical UCA size distribution. The resulting bandwidth is dictated by the transducer design, which in turn is dictated by the requirements of the clinical application. Thus, the sensitivity of contrast-enhanced ultrasound imaging and that of molecular imaging with bubbles and ultrasound[4] can be dramatically increased through the use of a narrowed down size distribution, or monodisperse bubbles, resonant to the frequency of the driving

ultrasound field. Moreover, the delivery of small molecule drugs and nucleic acids (e.g., siRNAs) to target cells using loaded microbubbles and ultrasound[5−9] will be more precise and efficient using bubbles that have a uniform acoustic response.

It has been demonstrated that bubble populations, monodisperse in terms of size, can be obtained by mechanical filtration,[10] decantation,[11] and centrifugation[12] of a polydisperse agent. Recently, it was demonstrated that microbubbles can be sorted with high precision in microfluidic devices; i.e., microbubbles can be sorted to size in a pinched micro-channel,[13] and they can be sorted to their acoustic property using the primary radiation force[14] induced by a traveling acoustic wave.[15] Another approach is to readily produce monodisperse bubbles in a flow-focusing device, a proven versatile tool for the highly controlled production of monodisperse bubbles.[16−18] In a flow-focusing device a gas thread is focused by two perpendicular flows through a narrow orifice where the gas experiences capillary instability and

pinches off to release monodisperse bubbles. Surfactant molecules are added to the co-flows to stabilize the newly formed bubbles against coalescence and dissolution. However, the hydrophobicity of phospholipid molecules promotes the formation of lipid aggregates in an aqueous solution, which hinders direct adsorption to the gas−liquid interface.[19,20] It was suggested that shear forces may disrupt the aggregates to facilitate adsorption.[21,22] However, questions remain as to where lipid adsorption takes place, the shear-rate dependency, and the conformation, or state, of the monomolecular film.

Once a bubble is formed in a saturated medium, it eventually dissolves due to the Laplace overpressure within the bubble owing to the finite surface tension of the curved gas−liquid interface.[20,22−24] Mechanical compression of the lipid monolayer results in a surface pressure high enough to counteract, or balance, the surface tension. Moreover, the diffusivity of gas molecules through the membrane decreases with monolayer compression to further stabilize the bubble.[25,26] The compressed solid-like shell of the mechanically stable bubble has viscoelastic properties that dramatically change the resonance behavior of the bubble.[27−29] The resonance frequency increases due to increased shell stiffness. Damping increases primarily due to shell viscous dissipation which decreases the resonance frequency typically by less than 2%.[30]

The medical application of monodisperse bubbles produced by flow-focusing requires high production rates, in the order of $10^5−10^6$ bubbles/s, to produce bubble suspensions with a clinically relevant bubble count, within a time frame of minutes. Moreover, it is evident that the microbubble filling gas is required to have a low aqueous solubility for prolonged microbubble persistence in vivo.[31] It was reported before that the monodispersity of microfluidically produced bubbles could only be maintained for nitrogen gas-filled[32] and air-filled[24] bubbles formed at low production rates. Bubble suspensions with a low-solubility gas, e.g., C_3F_8, and produced at high production rates, were shown to rapidly lose their monodispersity due to Ostwald ripening.[23] Here, we characterize the long-term size stability of perfluorobutane C_4F_{10} gas-filled bubbles produced in a flow-focusing device at high production rates, at up to 10^6 bubbles/s, and study the effects of shear-rate and mechanical compression on monolayer state, lipid adsorption, and resonance behavior. Moreover, the influence of repeated acoustic insonations on the physicochemical monolayer properties is also studied.

2. MATERIALS AND METHODS

2.1. Phospholipid Formulation. A Definity-like lipid mixture was used containing DPPC, DPPA, and DPPE-PEG5000 in a 80:10:10 molar ratio. The choice for this lipid formulation was driven by its observed ability to stabilize microbubbles formed at high production rates against coalescence directly after bubble formation.[33,34] The total lipid concentration was 10 mg/mL, and it was chosen such that no coalescence was observed even at the highest production rate; i.e., a lower lipid concentration led to bubble coalescence.

Lipids dissolved in chloroform (Avanti Polar Lipids, Alabaster, AL, USA) were mixed and dried on the wall of a glass vial under a stream of nitrogen gas and further dried overnight at a low ambient pressure. The lipid film was rehydrated in a 60 °C mixture of water (Milli-Q, Millipore Corp., Billerica, MA, USA), propylene glycol, and glycerol mixed in a 90:5:5 volume ratio (GPW mixture). Subsequently, the lipid solution was sonicated in a water bath at 60 °C for 30 min and stored at 4 °C. Prior to all experiments the lipid solution was sonicated by a tip sonicator for 1 min, degassed, and saturated with perfluorobutane C_4F_{10} gas.

2.2. Chip Fabrication. The molds for the polydimethylsiloxane (PDMS) chips were fabricated using standard soft lithography techniques.[35] In short, a layer of SU-8 photoresist was spin-coated on a silicon wafer and UV-exposed through a mask (MESA+ NanoLab, University of Twente) containing the channel features. This process was repeated for the chips containing two different channel heights. The second mask containing the higher channel features was carefully aligned with the lower channel features that were already exposed during the first UV exposure. Afterward, the wafer was developed to be ready for replica molding. PDMS was mixed in the standard 1:10 ratio, degassed, poured over the mold, and cured at 65 °C for 1 h, then cut to size. Fluidic ports were punched through the PDMS before the channels were sealed by bonding them to a microscope slide using a plasma cleaner (Harrick Plasma, Model PDC-002, Ithaca, NY, USA). Teflon tubing (PEEK, Upchurch) was connected to the inlet channels through which gas and liquid were supplied. The channels were filled with water (Milli-Q, Millipore) immediately after bonding to maintain their hydrophilicity. All chips used in this study contained an expanding nozzle flow-focusing geometry as was introduced by Tan et al.[36]

2.3. Imaging Setup. The imaging system consisted of an inverted microscope (Nikon Instruments, Eclipse TE2000-U) equipped with two objectives (20× and 60× magnification, Nikon Instruments, Plan Fluor ELWD) and an additional 1.5× magnification lens. Two cameras were connected to the microscope: a CCD camera (Lumenera, LM165M) with a pixel size of 6.45 μm and a high-speed camera (Photron SA1.1) with 20.0 μm pixel size. The recordings were processed with an automated image analysis algorithm programmed in MATLAB to obtain the sizes of the bubbles from the inflection point of their intensity profiles.[15]

2.4. Bubble Production. Microbubbles were produced in a flow-focusing device with a channel height of 13.6 μm and with a 7 μm wide nozzle that expanded to a 500 μm wide outlet channel (Figure 1A). A
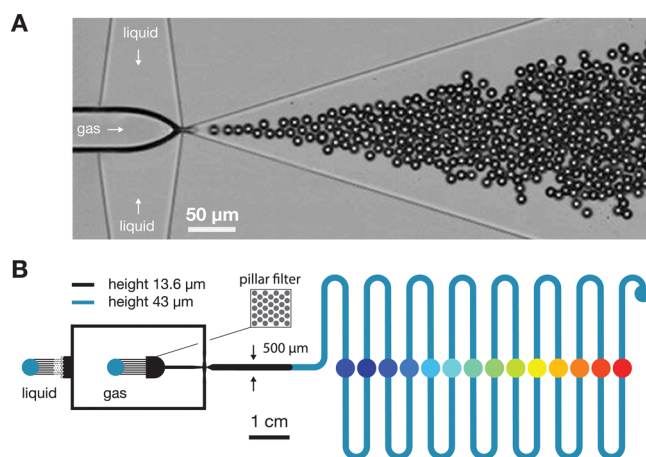

Figure 1. Bubble formation at a rate of 6×10^4 bubbles/s from a flow-focusing geometry (A) connected to a serpentine channel 15 cm in length (B) to characterize the bubble stability over the first minute after their formation.

serpentine channel 43 μm in height and with a total length of 15 cm was added downstream of the flow-focusing device to monitor bubble stability during the first minute after formation; see Figure 1B. Bubbles were formed at a C_4F_{10} gas (F2 Chemicals Ltd.) pressure of 1.08 bar that was controlled by a pressure regulator (Omega, PRG101-25) connected to a pressure sensor (Omega, DPG1000B-30G). The lipid suspension flow rate was 15 μL/min, and it was controlled by a high-precision syringe pump (Harvard Apparatus, PHD 2000, Holliston, MA, USA). The bubble size distribution in the serpentine channel was measured optically at a spatial resolution of 0.22 μm/pixel at 14 locations, marked by the colored dots in Figure 1B.

The size stability of the bubble suspension at the exit of the serpentine channel was further characterized by transferring a drop of
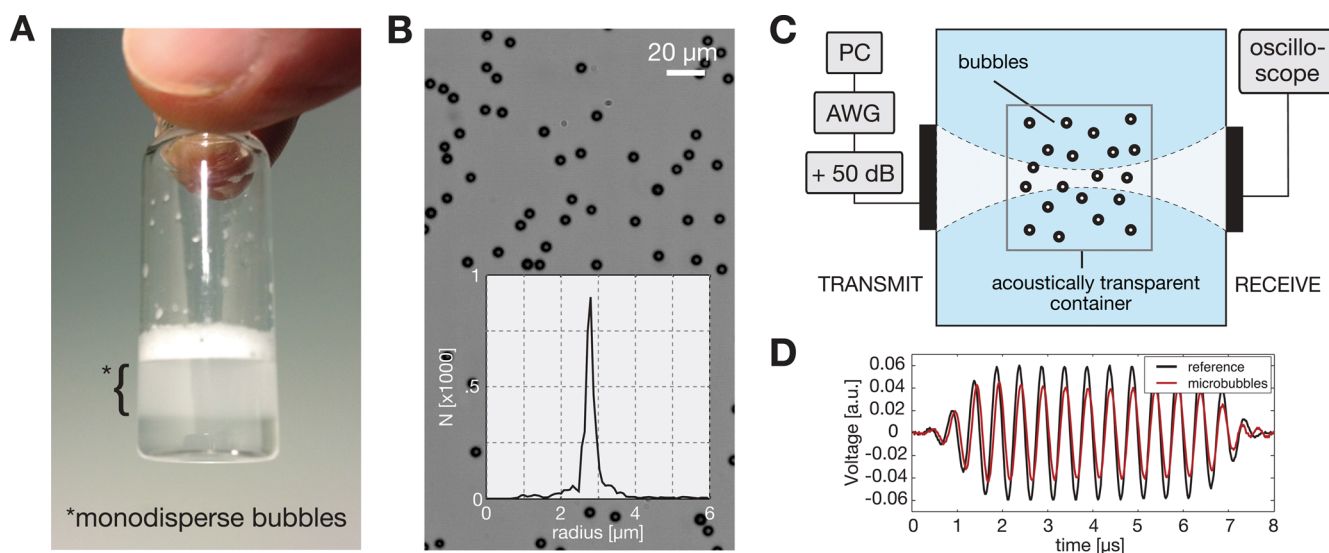
Figure 2. (A) Produced bubble suspension that was allowed to stabilize in a glass vial for 1.5 h after which it was gently mixed and set to rest for another 10 min. From the opaque layer of stabilized monodisperse bubbles (B) that appeared below the foam layer (see discussion on the size stability in section 3.1), bubbles are transferred to an acoustic characterization setup (C). Ultrasound pulses (D) with a frequency ranging from 0.7 to 5.5 MHz at 0.1 MHz intervals at peak negative pressures of 5−70 kPa in 2.5 kPa steps are transmitted through the bubble sample to measure the frequency- and pressure-dependent bubble resonance behavior.

the bubble suspension to a flow cell (IBIDI μ-slide). The bubble suspension in the flow cell was diluted with water (Milli-Q, Millipore) such that individual bubbles were visible. The flow cell was open to the atmosphere at both ends, and the liquid inside was stationary. Dissolution curves were obtained from images taken at 60 s time intervals over a 1.5 h period at a spatial resolution of 155 nm/pixel.

2.5. Nozzle Size and Flow Rates. The relation between the co-flow rate and the size stability of the bubbles was measured using co-flow rates ranging from 3 to 34 μL/min at C_4F_{10} gas pressures of 1.08 and 1.2 bar to produce bubbles of different initial sizes. Additionally, nozzle sizes of 3, 5, and 7 μm were used to produce bubbles in the same size range at different flow rates. The role of the filling gas was measured by the production of air-filled bubbles from a 5 μm nozzle, also at a gas pressure of 1.08 bar. The outlet channel of each flow-focusing device was straight, 13.6 μm in height, 500 μm in width, and 1.5 cm in length.

After setting the flow rate, the bubble formation was left to stabilize for at least 5 min. Then, the size and the production rate of the bubbles were measured using the high-speed camera operated at a frame rate of 225 kfps and at a spatial resolution of 0.67 μm/pixel.

The bubble suspensions produced at the outlet port of the flow-focusing device were pipetted, diluted in the GPW mixture, and transferred to a flow cell for optical sizing (108 nm/pixel resolution) over a 2 h time window at a time interval of 15 min. The bubble count for every size distribution was at least 1500.

2.6. Acoustic Characterization. The resonance behavior and acoustic stability of bubbles with an initial radius of 6.9 μm formed from a 5 μm nozzle (C_4F_{10} gas pressure = 1.08 bar, Q_{liq} = 13 μL/min) was characterized by narrow-band acoustic attenuation measurements. Attenuation was measured from a single ultrasound pulse per transmit frequency to minimize the effect that repeated insonations may have on the bubble response. A 100 μL aliquot of the bubble suspension was mixed with 2 mL of GPW mixture and set to rest. After 1.5 h the bubble suspension was stirred gently and set to rest for another 10 min. From the opaque layer below the foam (Figure 2A), 10 μL was pipetted and transferred to the sample cell of the acoustic characterization setup containing air-saturated water (Milli-Q, Millipore). The sample cell had a cross-sectional area of 1.5 × 1.5 cm^2, and it was made of acoustically transparent polystyrene membrane (Opticell). A magnetic stirrer bar inside the sample cell ensured a homogeneous bubble suspension during the measurements.

Another 10 μL was injected into a flow cell for optical sizing at a spatial resolution of 108 nm/pixel (Figure 2B).

Acoustic attenuation curves were measured using two co-aligned transducers[37] both with a focal distance of 25 mm and an aperture of 19 mm (transmit, A305S; receive, C308, Panametrics-NDT) in a water tank at 20 °C; see Figure 2C. The attenuation of a narrow-band 16-cycle ultrasound pulse (Figure 2D), with a four-cycle Gaussian tapering on each side of the pulse, traveling through the 1.5 cm bubble screen, was measured over a frequency range from 0.7 to 5.5 MHz with 0.1 MHz steps at acoustic pressures ranging from 5 to 70 kPa in steps of 2.5 kPa. A full measurement series consisted of 1323 driving pulses, of which the amplitude was compensated for the frequency-dependent transducer response that was measured with a calibrated 0.2 mm hydrophone (Precicion Acoustics), and were uploaded to a programmable arbitrary waveform generator (8026, Tabor Electronics) before the measurement. The driving pulses were amplified by 50 dB (350L, E&I), and the attenuated signals were recorded and stored in a digital storage oscilloscope (TDS5034B, Tektronix) operating in sequence mode. A complete scan was performed under 30 s.

3. RESULTS AND DISCUSSION

3.1. Size Stability. Figure 3A shows the optically measured size distributions at 14 different locations in the serpentine channel. The color of the size distribution plot corresponds to the color of the circle mark on the serpentine channel; it defines the location where the size distribution was measured. The inset in Figure 3A shows the total number of bubbles at each location measured from a set of 100 microscope recordings. The nearly constant bubble count shows that the freshly formed bubbles do not coalescence or fragment after formation. The bubbles were produced at an initial radius of 7.1 μm ± 0.2 μm, at a rate of 6 × 10^4 s^{-1} measured directly downstream from the nozzle using high-speed imaging. The total travel time of the bubbles through the serpentine channel was approximately 1 min. The bubble suspension became polydisperse in the serpentine channel, i.e., already within 10−15 s after formation (green size distribution in Figure 3A). However, upon reaching the end of the serpentine channel (red
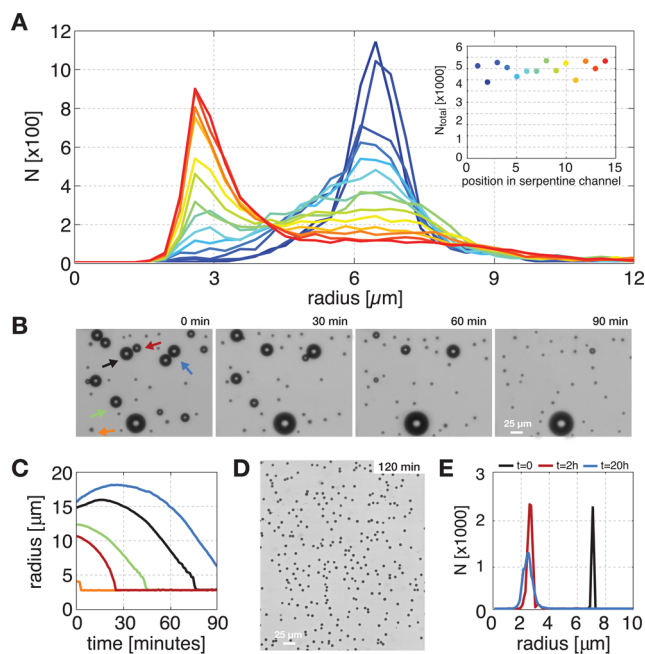
Figure 3. (A) Size distributions in the serpentine channel. The colors of the plots correspond to the colors of the circles marked on the serpentine channel in Figure 1B. (B) Dissolution of bubbles, initially formed at a radius of 7.1 μm, to a stable radius of 2.8 μm. (C) Dissolution curves of the bubbles in Figure 3B. The color of the curve corresponds to the bubble pointed at with an arrow of the same color. These bubbles increased in size during the first minute after production but dissolved all (D) to their stable radius of 2.8 μm. (E) Long-term size stability of bubbles initially produced at a radius of 7.1 μm.

size distribution plot), 60% of the bubbles had dissolved back into a monodisperse suspension with a bubble radius of 2.8 μm.

The size stability of the bubble suspension at the exit of the serpentine channel was further characterized over time in a flow cell. Figure 3B shows the dissolution of bubbles, initially formed at a radius of 7.1 μm, to a stable radius of 2.8 μm. The smallest bubbles in the suspension that did not reach their stable size yet (red arrow in Figure 3B), dissolve first and their gas is diffused into neighboring bubbles of a larger size (black arrow in Figure 3B). The dissolution stops when the bubble reaches its stable size by a lowering of the effective surface tension through a mechanical compression of the monolayer shell. The bubble that first grew in size (black arrow), acting as a sink for the stabilized bubble (red arrow), is now one of the smallest unstable bubbles in the suspension, which then allows for its own dissolution and stabilization (black curve in Figure 3B). This process is repeated until the gas that is lost by the stabilized bubbles is diffused into the initially largest bubble with the lowest Laplace pressure. This phenomenon is known as Ostwald ripening; however, in the presence of a stabilizing shell, these bubbles do not fully dissolve but reach a finite stable size (see Supporting Information movie). Figure 3C shows that some bubbles had more than doubled in size by reaching the end of the serpentine channel before eventually dissolving to the same final bubble radius of 2.8 μm. A microscope image with a larger field of view, captured 2 h after bubble formation, shows that even the biggest bubbles had dissolved to reach the same stable size; see Figure 3D. The size distribution of the stable bubbles, see $t = 2$ h in Figure 3E, shows that all bubbles reached a final bubble size that is 2.55 times smaller than the

initial bubble size formed at the nozzle; see $t = 0$ in Figure 3E. Thus, for this lipid formulation used at room temperature, the total number of phospholipid molecules on the bubble surface did not change after the formation of the bubble as adsorption or shedding of the shell material during the growth or shrinkage of a bubble would have resulted in a polydisperse bubble suspension. Moreover, the final bubble size was highly stable; see $t = 20$ h in Figure 3E, in the flow cell that was open to the atmosphere at both ends.

A simple thermodynamic analysis provides an explanation for the high lipid stability at the gas−water interface. The residence time (τ_r) of a lipid in a monolayer may be approximated by [see ref 38, p 545]:

$$\tau_r = 55\tau_0/\text{cmc} \qquad (1)$$

where cmc is the critical micelle concentration (M) and $\tau_0 = 10^{-7}$ s. Thus, the residence time of a DPPC lipid (cmc = 5 × 10^{-10} M) [see ref 38, p 518] is expected to be ≈3 h, which is longer than the time scale for Ostwald ripening observed under these conditions.

It was shown before that the polydispersity of bubbles produced in a flow-focusing device indeed increases within minutes due to Ostwald ripening.[19,23] It was also reported that the monodispersity of nitrogen-gas-filled bubbles[20] and air-filled bubbles[24] could be maintained by increasing the interbubble spacing, at the expense of the production rate. We speculate that a large interbubble spacing, i.e., a low bubble concentration, of bubbles filled with a gas having a high solubility in water results in the immediate dissolution of all formed bubbles to their stable size without noticeable Ostwald ripening resulting from the direct dissolution of the gas into the liquid. On the other hand, when bubbles are filled with a gas having a low aqueous solubility, the effect of Ostwald ripening cannot be avoided during the stabilization process. From the size ratio between the freshly formed bubbles and the stable bubbles, the liquid flow rate, and the production rate, it can be calculated that, in this particular case, per milliliter of bubble suspension, the unstable bubbles need to lose 0.23 mL of their filling gas. Thus, the initially unstable bubbles saturate the liquid rapidly with their filling gas after which the polydispersity is increased by Ostwald ripening. However, here we now show that, for the employed lipid formulation being used at room temperature, the suspension eventually converges to a monodisperse size determined by the original number of lipid molecules on the bubble surface. We expect that this long-term stabilization effect for heavy molecular weight gas-filled bubbles was left unnoticed in previous work due to the relatively long time scale of dissolution. We show that, in the confinement of the flow cell, the bigger bubbles, taking up the gas of the dissolving bubbles, in the end also dissolve to reach the same stable bubble size. We speculate that the C_4F_{10}-saturated liquid exchanges gas with the atmosphere at the open ends of the flow cell thereby facilitating the dissolution of the larger bubbles. The foam visible on top of the liquid layer in a vial of collected bubbles (Figure 2A) results from the observed Ostwald ripening during the stabilization process. The thickness of the foam layer was observed to decrease over time, expectedly due to a combination of gas exchange with the atmosphere and loss of the larger bubbles to the atmosphere due to their lower surfactant packing density.[39]

3.2. Flow-Rate Dependency. Panels A-1 to A-6 of Figure 4 show high-speed recordings of a 7 μm nozzle flow-focusing device operated at flow rates of 7, 19, 25, 28, 31, and
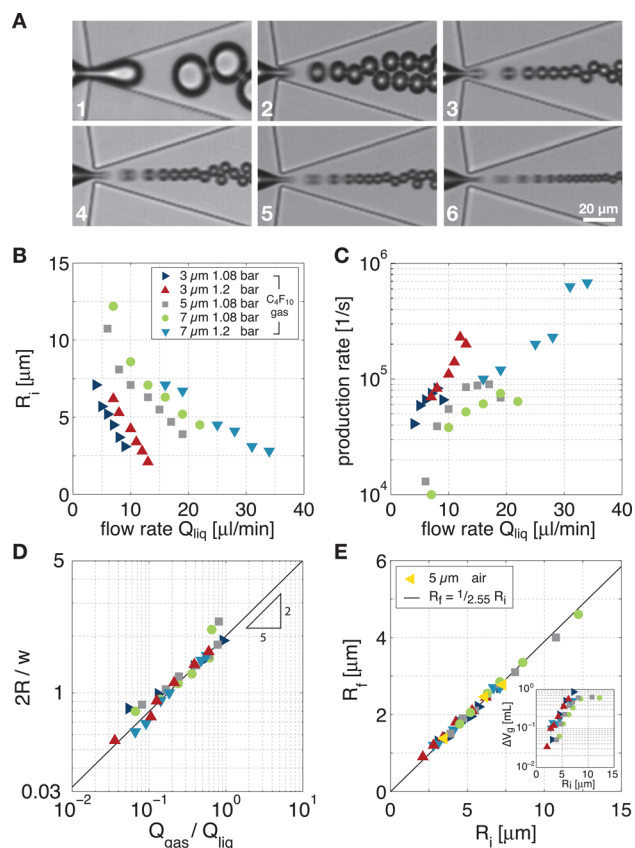
Figure 4. (A) Monodisperse bubble formation from a 7 μm nozzle at co-flow rates of 7, 19, 25, 28, 31, and 34 μL/min for panels A-1 to A-6 at gas pressures of 1.08 bar for panel A-1 and 1.2 bar for panels A2−A6. (B) Initial bubble radius R_i as a function of the co-flow rate for different nozzle sizes and gas pressures. (C) Bubble production rates as a function of the co-flow rate. (D) Bubble formation followed the scaling law for a planar flow-focusing device. (E) Final bubble radius R_f as a function of R_i for bubbles filled with perfluorobutane and for bubbles filled with air. All bubbles dissolve to a final radius 2.55 times smaller than their initial radius. The inset shows the gas loss per milliliter of bubble suspension that is needed to diffuse in order to dissolve all freshly formed bubbles into stable bubbles.

34 μL/min. The gas pressure in panel A-1 of Figure 4 was 1.08 bar, and in panels A-2 to A-6 of Figure 4 it was 1.20 bar. No coalescence was observed directly at the nozzle and in the outlet channel. The equivalent radii of bubbles compressed by the top and bottom walls of the outlet channel (e.g., Figure 4A-1) were calculated from a volume estimation based on the cross-sectional area of the compressed bubble calculated from the known channel height and measured bubble radius. The initial bubble radius R_i is plotted in Figure 4B as a function of the co-flow rate for different nozzle sizes and gas pressure combinations.

Figure 4C shows that bubbles are produced at a rate ranging from 10^4 to almost 10^6 s^{-1}. The production rate was used to calculate directly the gas flow rate, and Figure 4D shows that the bubble formation follows with good agreement the 2/5 scaling law for a planar flow-focusing device at high Reynolds numbers:[16] $2R/w \propto (Q_{gas}/Q_{liq})^{2/5}$ for $Q_{gas} < Q_{liq}$, where R is the radius of the bubble, w is the nozzle width, and Q_{gas} and Q_{liq} are the gas and liquid flow rates.

The formed bubbles were left to stabilize in a flow cell. The amount of gas exchange for bubbles to stabilize scales with the

volume of the bubble and with the pressure gradient across the surface, or Laplace pressure,[14] which decreases with $1/R$. As a result, the stabilization time scale for the smallest bubbles was on the order of minutes, while the larger bubbles reached their final size after 2 h. The final bubble radius R_f is plotted in Figure 4E as a function of R_i. A unique shear rate independent relation is found between R_i and R_f, where the final bubble size was always found to be 2.55 times smaller than the initial bubble size. Thus, the surface area of freshly produced bubbles ultimately decreases by a factor 6.6 to reach a stable size. It was reported that perfluorocarbon gases increase the rate of lipid adsorption on the gas−liquid interface with respect to air as a filling gas.[40,41] Here, we do not see an effect of the filling gas on the dissolution ratio; see the presented data for air-filled bubbles in Figure 4E. The total gas volume that needs to diffuse out of the freshly formed bubbles upon their stabilization, per milliliter of bubble suspension, is calculated from the production rate, the flow rate, and the dissolution ratio, and it is shown in the inset of Figure 4E. Please note that the aqueous solubility of perfluorobutane gas at room temperature and atmospheric pressure is only 1.5 μL/mL; this is up to 3 orders of magnitude lower than the gas volume lost by the freshly formed bubbles per milliliter of bubble suspension during bubble stabilization.

In the dripping regime[42] (Figure 4A-1), the gas thread blocks the nozzle, and as a consequence, bubbles drip from the nozzle and the gas thread is in contact with the top and bottom wall of the channel. Therefore, the only regions of high shear in the nozzle are the corners where the curved gas jet is not in contact with the rectangular nozzle.[43] In the jetting regime[42] (Figure 4A-6), the gas thread forms a jet that breaks up into bubbles downstream from the nozzle, and it was therefore fully surrounded by a high-shear flow. Since a flow rate and a production mechanism independent dissolution ratio was found, it can be concluded that the complete gas thread, or at least the tip of the gas thread that is subject to high-shear flow, is covered with a saturated surface concentration of the phospholipids. Thus, the lipid adsorption process has reached equilibrium before the bubble pinches off, even at the lowest flow rates used here, and the bubbles do not lose or adsorb lipids after their formation. Moreover, it can be concluded that the lipid adsorption time scale under all of these conditions is shorter than the time required for bubble formation (<1 μs).

Langmuir trough isotherms have shown that the surface pressure of DPPC monolayers reaches the surface tension of water when the monolayer is compressed to the condensed phase.[44,45] It is known that DPPC molecules in the subphase equilibrate with an air−water interface to form a liquid-expanded phase monolayer (surface tension $\approx$ 6 mN/m at 20 °C).[46] Lozano and Longo[47] showed that, for a lipid system with a 9:1 ratio of DPPC and DSPE-PEG2000, the surface tension approached zero when the monolayer was compressed from the start of the liquid-expanded to liquid-condensed phase transition to an area 6−8 times smaller (1.2−1.6 nm^2/molecule). This is in excellent agreement with the value of 6.6 that we found in our experiment. Thus, lipid molecules adsorb to the gas−liquid interface in the disordered expanded state, and then they become mechanically compressed by Laplace pressure-driven bubble dissolution to a more ordered condensed state with near zero surface tension.

3.3. Acoustic Characterization and Acoustic Stability.
Figure 5A shows the first series of 27 attenuation curves that were measured on the bubble sample with the size distribution
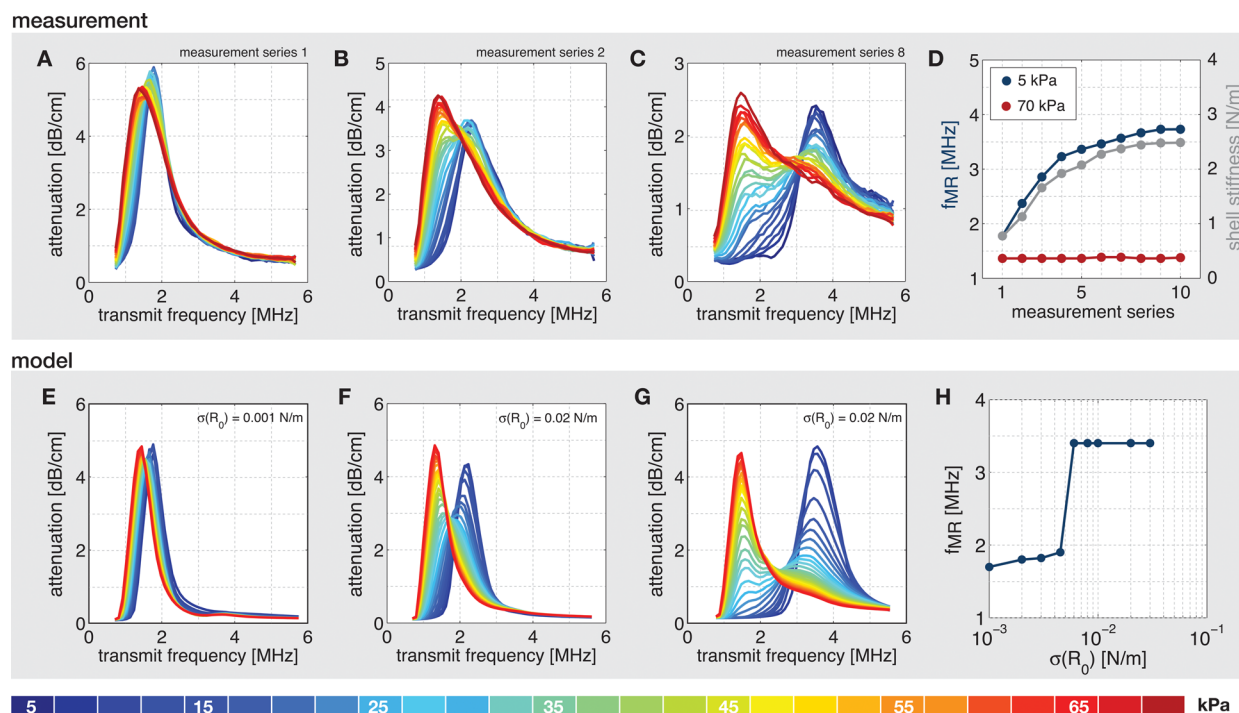
Figure 5. (A) First measurement series of 27 attenuation curves at peak negative acoustic pressures of 5−70 kPa. (B) Second measurement series. (C) Eight series. (D) Measured frequency of maximum response f_{MR} at a driving pressure of 5 kPa and at 70 kPa as a function of the measurement series. (E) Modeled attenuation curves for bubbles with $\sigma(R_0) = 0.001$ N/m and a shell elasticity of 2.5 N/m, (F) $\sigma(R_0) = 0.02$ N/m and shell elasticity 0.8 N/m, and (G) $\sigma(R_0) = 0.02$ N/m and shell elasticity 2.5 N/m. (H) Modeled frequency of maximum response at a driving pressure of 5 kPa as a function of the initial surface tension.

shown in Figure 2B. The measurement series was repeated 10 times on the very same bubble sample to measure the influence of repeated insonations on the response of the bubbles and, as such, its acoustic stability. The time between successive measurements was approximately 2 min. Figure 5B shows the second series, and Figure 5C shows the eighth series. The resonance frequency, or frequency of maximum response f_{MR}, at a driving pressure of 5 kPa increased with the number of insonations from 1.8 to 3.6 MHz (Figure 5D, blue dots). At 70 kPa, the f_{MR} remained constant for the whole series at a frequency of 1.4 MHz, indicating that the mean bubble size was unchanged during the multiple insonations since the resonance frequency of bubbles insonified at these relatively high acoustic pressures approaches that of free, uncoated bubbles.[27]

The increase in resonance frequency at low acoustic driving pressures may be explained both from an increase in shell elasticity or from an increase in the initial surface tension.[1,27] To quantify the change in the shell parameters with the number of insonations, we model the pressure-dependent attenuation of the bubble size distribution shown in Figure 2B with the model described in Segers et al. [48]. The attenuation is calculated by integration over the pressure-dependent echo response of all bubbles within the spatially nonuniform acoustic field of the transmit transducer. Figure 5E shows the modeled attenuation curves for bubbles with a shell stiffness of 2.5 N/m and an initial surface tension $\sigma(R_0)$ of 0.001 N/m. The shell viscosity was set to 6×10^{-9} kg/s. Increasing $\sigma(R_0)$ over a typical range of 0.001−0.030 N/m resulted in a rather abrupt change of the f_{MR} at a driving pressure of 5 kPa in our model; see Figure 5H, which is not in agreement with the experimentally observed monotonous increase of f_{MR} in Figure 5D. Panels F and G of Figure 5 show the modeled attenuation curves for bubbles with

a $\sigma(R_0)$ of 0.02 N/m and a shell stiffness of 0.8 and 2.5 N/m, respectively. The quantitative agreement with experiment thus reveals that the increasing f_{MR} at low driving pressures originates from an increasing shell stiffness. Over the 10 measurement series, the shell elasticity increased from 0.8 to 2.5 N/m as calculated from the linearized Rayleigh−Plesset equation;[27] see Figure 5D.

Lipid shedding has often been suggested[49,50] to occur during multiple insonations. From the critical micelle concentration ratio of DPPC to DPPE-PEG5000, it follows that the residence time (see eq 1) of a single DPPC molecule in the disordered monolayer of an expanded bubble is ≈30,000 times longer than that of a DPPE-PEG5000 molecule.[38] The van der Waals forces between lipid molecules in the solid-like, condensed shell of a stable microbubble are expected to be significant owing to the high lipid packing density. As a consequence, the DPPE-PEG5000 molecules are retained in the shell at rest. Forced oscillations of the microbubble and fluid microstreaming during insonation would likely decrease the molecular collision time (τ_0 in eq 1) in the monolayer, thereby accelerating lipid dissolution. As a result, the bubble shells become enriched in DPPC molecules. Since only 1 in 70 lipid molecules is DPPE-PEG5000, this loss is not expected to change the bubble size. However, it may have a direct effect on the acoustic properties of the bubble. Lozano and Longo[47] showed that the monolayer elasticity, obtained from the derivative of the surface pressure−area isotherm,[27] of a DPPC:DPPE-PEG2000 monolayer increases with decreasing DPPE-PEG2000 fraction. Moreover, Dicker et al.[51] show that the average shell stiffness of microbubbles coated with a 7.5 mol % fraction of DSPE-PEG5000 molecules is much lower than that of bubbles coated with a 1 mol % fraction of DSPE-PEG5000. Thus, the loss of

emulsifier molecules results in a gradually increasing shell stiffness as observed directly from Figure 5D. The presented control over the size stability and nonlinear acoustic response of microbubbles formed by flow-focusing at high production rates possibly allows for an increased sensitivity and efficiency in contrast-enhanced ultrasound imaging. Moreover, it has the potential to boost emerging applications such as molecular imaging and drug delivery with ultrasound.

4. CONCLUSIONS

Phospholipid-coated perfluorobutane gas-filled microbubbles produced in a flow-focusing device with a DPPC:DPPA:DPPE-PEG5000 lipid formulation at a total lipid concentration of 10 mg/mL are stable once they have dissolved to a radius that is 2.55 times smaller than their initial radius. The lipid adsorption process reaches equilibrium before the bubble pinches off and the amount of phospholipids on the bubble surface does not change after bubble formation, not when the bubble dissolves, nor when it expands volumetrically. The size stability is independent of the flow-focusing nozzle shear rate and production rate. It was shown that monodisperse bubbles can be produced with a rate up to 1 million bubbles per second from a single nozzle. Attenuation measurements together with modeled attenuation curves in which the full nonlinear bubble response was included revealed that the average shell stiffness of the bubbles increased from 0.8 to 2.5 N/m with increasing number of insonations due to the loss of emulsifier molecules.

■ ASSOCIATED CONTENT

Ⓢ Supporting Information

The Supporting Information is available free of charge on the ACS Publications website at DOI: 10.1021/acs.langmuir.6b00616.

Stabilization process of initially monodisperse microbubbles formed by flow-focusing (AVI)

■ AUTHOR INFORMATION

Corresponding Author

*E-mail: timsegers1@hotmail.com (T.S.); m.versluis@utwente.nl (M.V.).

Notes

The authors declare no competing financial interest.

■ ACKNOWLEDGMENTS

■ REFERENCES

(1) Overvelde, M.; Garbin, V.; Sijl, J.; Dollet, B.; de Jong, N.; Lohse, D.; Versluis, M. Nonlinear shell behavior of phospholipid-coated microbubbles. *Ultrasound Med. Biol.* **2010**, *36*, 2080−2092.

(2) Lindner, J. R. Microbubbles in medical imaging: current applications and future directions. *Nat. Rev. Drug Discovery* **2004**, *3*, 527−533.

(3) Minnaert, M. On musical air-bubbles and the sound of running water. *Philos. Mag.* **1933**, *16*, 235−248.

(4) Klibanov, A. L. Microbubble Contrast Agents: Targeted ultrasound imaging and ultrasound-assisted drug-delivery applications. *Invest. Radiol.* **2006**, *41*, 354−362.

(5) Carson, A. R.; McTiernan, C. F.; Lavery, L.; Grata, M.; Leng, X.; Wang, J.; Chen, X.; Villanueva, F. S. Ultrasound-targeted microbubble destruction to deliver siRNA cancer therapy. *Cancer Res.* **2012**, *72*, 6191−6199.

(6) Hernot, S.; Klibanov, A. L. Microbubbles in ultrasound-triggered drug and gene delivery. *Adv. Drug Delivery Rev.* **2008**, *60*, 1153−1166.

(7) Tsutsui, J. M.; Xie, F.; Porter, R. T. The use of microbubbles to target drug delivery. *Cardiovasc. Ultrasound* **2004**, *2*, 23.

(8) Deelman, L. E.; Decléves, A. E.; Rychak, J. J.; Sharma, K. Targeted renal therapies through microbubbles and ultrasound. *Adv. Drug Delivery Rev.* **2010**, *62*, 1369−1377.

(9) Dewitte, H.; Vanderperren, K.; Haers, H.; Stock, E.; Duchateau, L.; Hesta, M.; Saunders, J. H.; De Smedt, S. C.; Lentacker, I. Theranostic mRNA-loaded Microbubbles in the Lymphatics of Dogs: Implications for Drug Delivery. *Theranostics* **2015**, *5*, 97−109.

(10) Emmer, M.; Vos, H. J.; Goertz, D. E.; van Wamel, A.; Versluis, M.; de Jong, N. Pressure-dependent attenuation and scattering of phospholipid-coated microbubbles at low acoustic pressures. *Ultrasound Med. Biol.* **2009**, *35*, 102−111.

(11) Goertz, D. E.; de Jong, N.; van der Steen, A. F. W. Attenuation and size distribution measurements of definity and manipulated definity populations. *Ultrasound Med. Biol.* **2007**, *33*, 1376−1388.

(12) Feshitan, J. A.; Chen, C. C.; Kwan, J. J.; Borden, M. A. Microbubble size isolation by differential centrifugation. *J. Colloid Interface Sci.* **2009**, *329*, 316−324.

(13) Kok, M. P.; Segers, T.; Versluis, M. Bubble sorting in pinched microchannels for ultrasound contrast agent enrichment. *Lab Chip* **2015**, *15*, 3716−3722.

(14) Leighton, T. G. *The Acoustic Bubble*; Academic Press: London, 1994.

(15) Segers, T.; Versluis, M. Acoustic bubble sorting for ultrasound contrast agent enrichment. *Lab Chip* **2014**, *14*, 1705−1714.

(16) Gañán-Calvo, A. M.; Gordillo, J. M. Perfectly monodisperse microbubbling by capillary flow focusing. *Phys. Rev. Lett.* **2001**, *87*, 274501.

(17) Anna, S. L.; Bontoux, N.; Stone, H. A. Formation of dispersions using "flow focusing" in microchannels. *Appl. Phys. Lett.* **2003**, *82*, 364−366.

(18) Garstecki, P.; Stone, H. A.; Whitesides, G. M. Mechanism for Flow-Rate Controlled Breakup in Confined Geometries: A Route to Monodisperse Emulsions. *Phys. Rev. Lett.* **2005**, *94*, 164501.

(19) Hettiarachchi, K.; Talu, E.; Longo, M. L.; Dayton, P. A.; Lee, A. P. On-chip generation of microbubbles as a practical technology for manufacturing contrast agents for ultrasonic imaging. *Lab Chip* **2007**, *7*, 463−468.

(20) Talu, E.; Hettiarachchi, K.; Powell, R. J.; Lee, A. P.; Dayton, P. A.; Longo, M. L. Maintaining monodispersity in a microbubble population formed by flow-focusing. *Langmuir* **2008**, *24*, 1745−1749.

(21) Wang, K.; Lu, Y. C.; Xu, J. H.; Luo, G. S. Determination of Dynamic Interfacial Tension and Its Effect on Droplet Formation in the T-Shaped Microdispersion Process. *Langmuir* **2009**, *25*, 2153−2158.

(22) Kwan, J. J.; Borden, M. A. Lipid monolayer collapse and microbubble stability. *Adv. Colloid Interface Sci.* **2012**, *183-184*, 82−99.

(23) Shih, R.; Bardin, D.; Martz, D. T.; Sheeran, P. S.; Dayton, P. A.; Lee, A. P. Flow-focusing regimes for accelerated production of monodisperse drug-loadable microbubbles toward clinical-scale applications. *Lab Chip* **2013**, *13*, 4816−4826.

(24) Shih, R.; Lee, A. P. Post-formation shrinkage and stabilization of microfluidic bubbles in lipid solution. *Langmuir* **2016**, *32*, 1939.

(25) Wheatley, M. A.; Singhal, S. Structural studies on stabilized microbubbles: development of a novel contrast agent for diagnostic ultrasound. *React. Polym.* **1995**, *25*, 157−166.

(26) Borden, M. A.; Longo, M. L. Oxygen permeability of fully condensed lipid monolayers. *J. Phys. Chem. B* **2004**, *108*, 6009−1344.

(27) Marmottant, P.; Van Der Meer, S.; Emmer, M.; Versluis, M.; De Jong, N.; Hilgenfeldt, S.; Lohse, D. A model for large amplitude oscillations of coated bubbles accounting for buckling and rupture. *J. Acoust. Soc. Am.* **2005**, *118*, 3499−3505.

(28) Sarkar, K.; Shi, W. T.; Chatterjee, D.; Forsberg, F. Characterization of ultrasound contrast microbubbles using in vitro experiments and viscous and viscoelastic interface models for encapsulation. *J. Acoust. Soc. Am.* **2005**, *118*, 539−550.

(29) Church, C. C. The effect of an elastic solid surface layer on the radial pulsation of gas bubbles. *J. Acoust. Soc. Am.* **1995**, *97*, 1510−1521.

(30) Van Der Meer, S.; Dollet, B.; Voormolen, M.; Chin, C. T.; Bouakaz, A.; De Jong, N.; Versluis, M.; Lohse, D. Microbubble spectroscopy of ultrasound contrast agents. *J. Acoust. Soc. Am.* **2007**, *121*, 648−656.

(31) Segers, T.; de Jong, N.; Lohse, D.; Versluis, M. Microbubbles for medical applications. *Microfluidics for Medical Applications*; RSC Nanoscience and Nanotechnology, Vol. 36; Royal Society of Chemistry: London, 2015; DOI: 10.1039/9781849737593.

(32) Talu, E.; Powell, R. L.; Longo, M. L.; Dayton, P. A. Needle size and injection rate impact on microbubble contrast agent population. *Ultrasound Med. Biol.* **2008**, *34*, 1182−1185.

(33) de Rond, L. Characterization of phospholipid-coated monodisperse microbubbles for medical imaging, Master's thesis, University of Twente, The Netherlands, 2014.

(34) Segers, T.; van Rooij, T.; de Rond, L.; Kooiman, K.; Dewitte, H.; Lentacker, I.; de Jong, N.; Versluis, M. Phospholipid formulation dependent bubble formation in microfluidic flow-focusing 2016, manuscript in preparation.

(35) Duffy, D. C.; McDonald, J. C.; Schueller, O. J. A.; Whitesides, G. M. Rapid prototyping of microfluidic systems in poly-(dimethylsiloxane). *Anal. Chem.* **1998**, *70*, 4974−4984.

(36) Tan, Y. C.; Cristini, V.; Lee, A. P. Monodispersed microfluidic droplet generation by shear focusing microfluidic device. *Sens. Actuators, B* **2006**, *114*, 350−356.

(37) Chen, Q.; Zagzebski, J.; Wilson, T.; Stiles, T. Pressure-dependent attenuation in ultrasound contrast agents. *Ultrasound Med. Biol.* **2002**, *28*, 1041−1051.

(38) Israelachvili, J. N. *Intermolecular and Surface Forces*, Vol. 2; Academic Press: Waltham, MA, USA, 1992.

(39) Postema, M.; Marmottant, P.; Lancee, C. T.; Hilgenfeldt, S.; de Jong, N. Ultrasound-induced microbubble coalescence. *Ultrasound Med. Biol.* **2004**, *30*, 1337−1344.

(40) Szijjarto, C.; Rossi, S.; Waton, G.; Krafft, M. P. Effects of perfluorocarbon gases on the size and stability characteristics of phospholipid-coated microbubbles: Osmotic effect versus interfacial film stabilization. *Langmuir* **2012**, *28*, 1182−1189.

(41) Nguyen, P. N.; Trinh Dang, T.; Waton, G.; Vandamme, T.; Krafft, M. A nonpolar, nonamphiphilic molecule can accelerate adsorption of phospholipids and lower their surface tension at the air/water interface. *ChemPhysChem* **2011**, *12*, 2646−2652.

(42) Utada, A. S.; Fernandez-Nieves, A.; Stone, H. A.; Weitz, D. A. Dripping to jetting transitions in coflowing liquid streams. *Phys. Rev. Lett.* **2007**, *99*, 094502.

(43) van Steijn, V.; Kreutzer, M. T.; Kleijn, C. R. μpiv study of the formation of segmented flow in microfluidic T-junctions. *Chem. Eng. Sci.* **2007**, *62*, 7505−7514.

(44) Nino, M. R. R.; Lucero, A.; Patino, J. M. R. Relaxation phenomena in phospholipid monolayers at the air-water interface. *Colloids Surf., A* **2008**, *320*, 260−270.

(45) Ma, G.; Allen, H. C. DPPC Langmuir Monolayer at the Air-Water Interface: Probing the Tail and Head Groups by Vibrational Sum Frequency Generation Spectroscopy. *Langmuir* **2006**, *22*, 5341−5349.

(46) Lee, S.; Kim, D. H.; Needham, D. Equilibrium and dynamic interfacial tension measurements at microscopic interfaces using a micropipet technique. 2. dynamics of phospholipid monolayer formation and equilibrium tensions at the water-air inteface. *Langmuir* **2001**, *17*, 5544−5550.

(47) Lozano, M. M.; Longo, M. L. Complex formation and other phase transformations mapped in saturated phosphatidylcholine/DSPE-PEG2000 monolayers. *Soft Matter* **2009**, *5*, 1822−1834.

(48) Segers, T.; de Jong, N.; Versluis, M. Uniform scattering and attenuation of acoustically sorted ultrasound contrast agents: modelling and experiments. Submitted for publication, 2015.

(49) O'Brien, J.-P.; Ovenden, N.; Stride, E. Accounting for the stability of microbubbles to multi-pulse excitation using a lipid-shedding model. *J. Acoust. Soc. Am.* **2011**, *130*, 180−185.

(50) Luan, Y.; Lajoinie, G.; Gelderblom, E.; Skachkov, I.; van der Steen, A. F. W.; Vos, H. J.; Versluis, M.; de Jong, N. Lipid shedding from single oscillating microbubbles. *Ultrasound Med. Biol.* **2014**, *40*, 1834−1846.

(51) Dicker, S.; Mleczko, M.; Siepmann, M.; Wallace, N.; Sunny, Y.; Bawiec, C. R.; Schmitz, G.; Lewin, P.; Wrenn, S. P. Influence of shell composition on the resonance frequency of microbubble contrast agents. *Ultrasound Med. Biol.* **2013**, *39*, 1292−1302.